Check for updates

Integration of multiwalled carbon nanotubes with MoS₂/BiFeO₃: a hybrid matrix for high-energy asymmetric supercapacitors

Eman A. Alabdullkarem,[a] Junaid Khan ✶[bce] and Hussein Alrobei[d]

Perovskite-structured bismuth ferrite (BiFeO₃, BFO) possesses considerable promise as a pseudo-capacitive material due to its enhanced theoretical capacitance. Nevertheless, its use is constrained by low electrical conductance and limited ion diffusion rates. To address these challenges, a ternary nanomaterial was constructed by integrating bismuth ferrite (BFO) with molybdenum disulfide (MoS₂) and multiwalled carbon nanotubes, resulting in a BiFeO₃/MoS₂@MWCNT hybrid electrode architecture specifically engineered for asymmetric supercapacitor devices. The inclusion of MoS₂ introduces numerous reactive sites for faradaic processes, while MWCNTs enhance the overall conductive and architectural properties of the hybrid matrix. Electrochemical testing revealed that the composite electrode achieves a specific capacitance of 1765 F g⁻¹ at 1 A g⁻¹ while exhibiting consistent performance across multiple scan rates. Assembled into a full ASC device using AC as the anode, the system delivers an impressive specific energy of 65.7 Wh kg⁻¹ at the rate of 802.7 W kg⁻¹. Moreover, a retention of 96.7% was observed after 10 k cycles. The superior electrochemical behaviour is owing to the combined effect of BiFeO₃, MoS₂, and MWCNTs, facilitating efficient charge transfer and stable ion transport pathways. This investigation reveals a promising technique for designing advanced composite electrodes for high-efficiency energy storage applications.

1. Introduction

The relentless advancement of portable electronics, electric vehicles, and renewable energy infrastructures has precipitated an unprecedented global demand for high-performance energy storage technologies. Supercapacitors, also known as electrochemical capacitors, have emerged as a pivotal class of devices capable of bridging the critical performance gap between conventional dielectric capacitors and batteries. Their exceptional attributes—including ultra-high power density, rapid charge-discharge kinetics, and outstanding cycle life—make them indispensable for applications requiring quick energy bursts and reliable long-term operation.[1,2] However, the relatively low energy density of commercial supercapacitors

remains a significant impediment to their broader application. In the pursuit of overcoming this fundamental limitation, asymmetric supercapacitors (ASCs) have been engineered as a sophisticated architectural solution. An ASC device strategically pairs a high-capacity, battery-type faradaic electrode (as the energy source) with a high-rate, capacitive electrode (as the power source) within a compatible electrolyte. This configuration allows the device to operate over a significantly expanded voltage window, which is paramount since the energy density (*E*) scales with the square of the voltage. Consequently, ASCs successfully amalgamate the high-energy characteristics of batteries with the high-power and durable performance of supercapacitors, presenting a compelling pathway for next-generation energy storage.[3–5]

The performance ceiling of any supercapacitor is intrinsically dictated by the properties of its constituent electrode materials. Traditional symmetric devices based on carbonaceous materials (*e.g.*, activated carbon) rely solely on the physical adsorption/desorption of ions (electrical double-layer capacitance, EDLC), which inherently limits their energy storage capacity. This has catalyzed intensive research into pseudocapacitive materials, which undergo fast, reversible surface redox reactions, thereby storing substantially more charge than EDLC materials. Among these, transition metal oxides (TMOs) have

[a] *Department of Chemistry, College of Science, King Saud University, P. O. Box 2455, Riyadh, 11451, Saudi Arabia*

[b] *Department of Physics, Government Postgraduate College No. 1, Abbottabad, Khyber Pakhtunkhwa, Pakistan. E-mail: junaidkhan.nanotech@gmail.com*

[c] *Department of Higher Education Achieves and Libraries, Government of Khyber Pakhtunkhwa, Pakistan*

[d] *Department of Mechanical Engineering, College of Engineering, Prince Sattam Bin Abdul Aziz University, Al-Kharj, 11942, Saudi Arabia*

[e] *Department of Chemical and Biological Engineering, Gachon University, 1342 Seongnam-daero, Seongnam 13120, Republic of Korea*

been extensively investigated due to their rich redox chemistry. Nevertheless, conventional TMOs such as RuO_2, NiO, and Co_3O_4 are often plagued by prohibitive cost, environmental toxicity, and limited potential windows, constraining their practical viability.[5,6] Other transition metal oxides like $Ni(OH)_2$, NiO and ZnO are less efficient in storage capability, operating voltage range and cost effectiveness.[7,8]

In light of these challenges, perovskite-based oxides with the general formula ABO_3 have recently surged to the forefront of materials research for advanced electrochemical energy storage. Originally prominent in fields like catalysis and solid oxide fuel cells, perovskites possess a highly versatile and stable crystal structure. Their robust framework can host a high concentration of oxygen vacancies and cation substitutions, which serve as highly active sites for faradaic reactions. This, combined with their intrinsic mixed ionic–electronic conductivity, renders them exceptionally suitable for pseudocapacitive charge storage. Seminal works on perovskites such as $LaMnO_3$, $LaCoO_3$, and $SrRuO_3$ have demonstrated their considerable potential, showcasing high specific capacitances and excellent rate capabilities derived from their unique electronic structure and compositional tunability.[7–9] A significant material within this group is bismuth ferrite ($BiFeO_3$), a perovskite oxide exhibiting multiferroic characteristics and demonstrating inherent electrochemical activity.[9,10] The BFO system can exist in several crystalline phases—each capable of reversible electrochemical phase transformations that can potentially augment its charge storage mechanism. Although the use of nanostructured BFO in supercapacitors is a relatively nascent area of research, initial investigations have confirmed its efficacy as a pseudocapacitive electrode, justifying more in-depth study.[11–13] For instance, work by Xiaoyu Li et al.[14] demonstrated a BFO-based hybrid supercapacitor achieving a gravimetric specific capacitance (C_s) of 61 F g^{-1} at 1 A g^{-1}. In a separate study,[15] BFO was reported to deliver a C_s of 105 F g^{-1} along with high energy density. Further supporting this, Shungao Yin et al.[16] showed that a BFO nanoplate based material attained a C_s of 254.6 F g^{-1}, in addition to exceptional cycling stability.

While bismuth ferrite ($BiFeO_3$) exhibits intrinsic pseudocapacitive behavior and multifunctionality, its practical use is severely limited by a fundamental drawback: very low electrical conductivity. This inherent property leads to unsatisfactory rate capability, impedes efficient charge mobility, and yields a specific capacitance that is too low for the material to be effective when used alone.[17] A principal method to overcome these deficiencies involves integrating highly conductive substances, especially transition metal sulfides, into the material structure. Molybdenum disulfide (MoS_2), a two-dimensional material with a layered architecture, has attracted significant attention in this context due to its high electrical conductivity, extensive surface area, and high density of sites available for electrochemical reactions.[18,19] Creating a composite of $BiFeO_3$ and MoS_2 capitalizes on a beneficial synergy of pseudocapacitive nature of BFO and exceptional conductivity of MoS_2. The resultant matrix will enable efficient charge transmission and ion dissemination, as well as establishes a dual-mechanism

energy storage system that incorporates both redox and electric double-layer capacitive (EDLC) processes. As a result, the $BiFeO_3/MoS_2$ composite shows a substantial increase in specific capacitance, better performance at high current rates, and exceptional longevity over many charge–discharge cycles.[20] This performance enhancement through synergy is supported by several studies on metal ferrite–MoS_2 combinations.[21–24] For instance, Samira Sharifi et al.[21] reported a specific capacitance (C_s) of 1013 F g^{-1} at 1 A g^{-1} for a $CoFe_2O_4/MoS_2$ composite.

To further boost the electrochemical performance of the multi-walled carbon nanotubes (MWCNTs), integrated $BiFeO_3/MoS_2$ is introduced. Within this system, the MWCNTs act as a highly effective conductive scaffold, creating a network that interconnects the electroactive $BiFeO_3$ and MoS_2 and ensures swift electron movement across the entire electrode matrix. The characteristically large surface area of the MWCNTs enhances interaction with the electrolyte, allowing for more efficient ion diffusion, while their inherent mechanical robustness helps maintain the electrode's structural stability throughout prolonged cycling.[25] This three-component integration is anticipated to markedly augment the composite's specific capacitance, ensuring a more efficient response at high current rates, and improving its ability to retain capacity, thereby outperforming simpler binary composites. The efficacy of incorporating MWCNTs is well-documented in the literature; for instance, studies consistently show that mixing metal oxides with MWCNTs leads to significant gains in electrochemical properties due to synergistic interactions.[26] The MXene/$BiFeO_3$/CNT electrode reported by S. Zainab achieved a C_s of 942.8 F g^{-1} at 1 A g^{-1} and a remarkable energy density of 231 Wh kg^{-1}.[27]

Given the documented developments, such as those reported in ref. 28–30, the engineering of multi-constituent nanostructured composites has emerged as a highly viable method for overcoming the performance constraints of single-component electrode materials. This research proposes a ternary $BiFeO_3/MoS_2$/MWCNT hybrid architecture, which is designed to harness the collective properties of its constituents: the distinct pseudocapacitance of $BiFeO_3$, the two-dimensional configuration and redox contribution of MoS_2, as well as the exceptional electrical conductivity and charge transport network provided by MWCNTs. The synergistic interplay among these components is anticipated to boost charge storage capabilities substantially. Consequently, this study concentrates on the synthesis, along with a comprehensive analysis of the obtained performance of the composite to assess its potential as a high-performance electrode material for next-generation supercapacitor devices. The cumulative benefits offered by each integrated material are projected to yield superior results.

2. Methodology

2.1 Preparation of the composite

The synthesis of the $BiFeO_3/MoS_2$ composite was accomplished through a sequential two-stage hydrothermal procedure. The first step involved the dissolution of 0.002 mol of $Fe(NO_3)_3$·

$9H_2O$ and 0.001 mmol of $Bi(NO_3)_3 \cdot 5H_2O$ in 0.05 L of a 2 M potassium hydroxide solution. This mixture was subjected to magnetic stirring for one hour to achieve a homogenous precursor solution. Subsequently, the solution was sealed within a Teflon-lined stainless-steel autoclave and underwent a hydrothermal reaction at 200 °C for a duration of 6 hours. The solid product obtained from this reaction was then isolated *via* filtration, meticulously washed and finally calcined at 400 °C for 2 hours to yield the pure $BiFeO_3$ phase.[31,32]

In the subsequent step, a precursor solution for molybdenum disulfide was prepared by dissolving 0.5 g of $Na_2MoO_4 \cdot 2H_2O$ and 0.4 g of thiourea (CH_4N_2S) in 100 mL of deionized water under continuous magnetic stirring. The pre-synthesized $BiFeO_3$ powder was then introduced into this solution, and the mixture was ultrasonicated for 30 minutes to ensure a uniform dispersion and suspension of the particles. This suspension was transferred to a 100 mL autoclave and subjected to a second hydrothermal treatment, this time at 180 °C for 36 hours. The final $BiFeO_3/MoS_2$ composite was collected, resulting in a composite with a mass ratio of 50 wt% for each component.[33]

For the purpose of comparison, the ternary $BiFeO_3/MoS_2$@MWCNT hybrid material was fabricated by following the same synthetic pathway with the inclusion of multi-walled carbon nanotubes. Specifically, prior to the second hydrothermal step, a predetermined amount of MWCNTs was dispersed in deionized water using 30 minutes of ultrasonication. This dispersion was then blended with the $BiFeO_3$-containing mixture to integrate the carbon nanotubes into the structure, achieving a final mass ratio of 85 wt% $BiFeO_3/MoS_2$ to 15 wt% MWCNTs. A schematic illustration depicting the proposed structural formation mechanism for both the binary and ternary materials is provided in Fig. S1 (SI).

2.2 Electrochemical studies

The electrochemical characterizations were performed in three-electrode and two-electrode cell configurations. For the three-electrode measurements, the working electrodes were fabricated from the $BiFeO_3/MoS_2$ and $BiFeO_3/MoS_2$@MWCNT composites. A platinum mesh and an Ag/AgCl electrode were employed as the counter and reference electrodes, respectively. To prepare the working electrodes, a homogeneous mixture was created by combining the active material (80 wt%) with conductive acetylene black (10 wt%) and polyvinylidene fluoride (PVDF) binder (10 wt%). A few drops of *N*-methyl-2-pyrrolidone (NMP) were added to this blend to form a consistent slurry, which was then applied onto nickel foam (NF) current collectors. The electrodes were subsequently dried, yielding a final active material loading of 2.3 mg per square centimeter. For the symmetric supercapacitor device, a two-electrode setup was assembled using the $BiFeO_3/MoS_2$@MWCNT composite as the cathode and an activated carbon (AC) electrode as the anode. Filter paper, which served as the separator, was first soaked in electrolyte for 2 hours, dried, and then carefully placed between the two electrodes to complete the device assembly.[34]

3. Structural and morphological aspects

The crystalline phase and structural purity of the synthesized samples were characterized using X-ray diffraction (XRD), with the results presented in Fig. 1a. The XRD profile for the $BiFeO_3/MoS_2$ composite reveals characteristic peaks of $BiFeO_3$ at 2θ angles of 22.4°, 31.8°, 39.4°, 51.0°, 51.7°, 71.3°, and 75.5°. These diffraction signals are indexed to the (012), (104), (202), (116), (122), (036), and (128) crystallographic planes, respectively. The pattern aligns well with a rhombohedral perovskite structure possessing *R3c* symmetry for BFO, matching the standard JCPDS file no. 86-1518.[35] Concurrently, the pattern exhibits broader peaks at 14.3°, 32.7°, 39.7°, 44.1°, and 59.0°, which are assigned to the (002), (100), (103), (006), and (110) planes of hexagonal MoS_2. The presence of these peaks verifies the
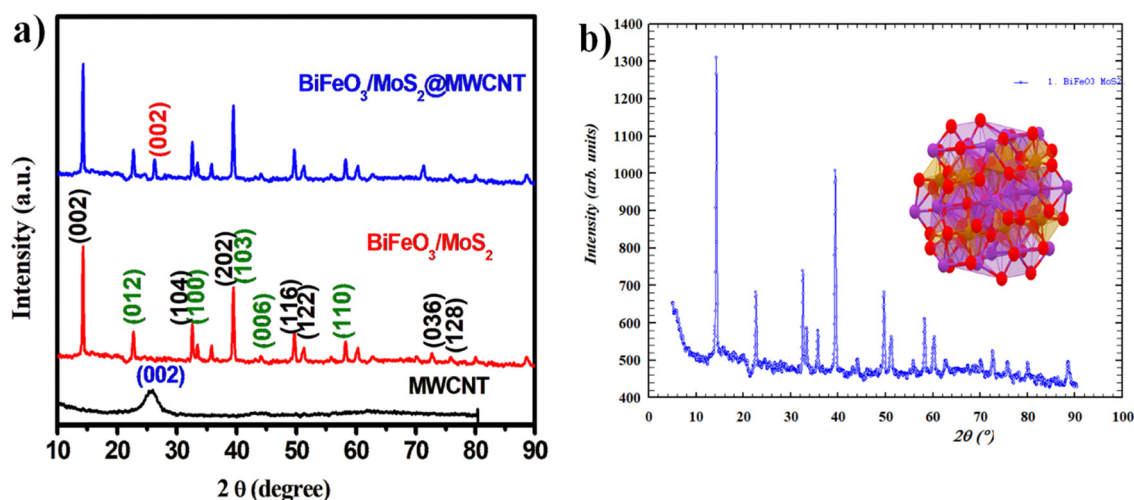

Fig. 1 (a) X-ray diffraction of both composites; (b) Rietveld refinement pattern for the composite, with the inset illustrating the corresponding crystal structure.

successful formation and integration of MoS_2 (JCPDS card no. 37-1402).

In the XRD pattern of the ternary $BiFeO_3/MoS_2$@MWCNT hybrid, a distinct additional peak emerges at 25.8°. This peak is characteristic of the (002) plane of graphitic carbon (JCPDS card no. 01-075-1621) in the MWCNTs. Its presence confirms the incorporation of the carbon based material and indicates that the MWCNTs were integrated without inducing significant alterations to the inherent crystalline structures of the $BiFeO_3/MoS_2$ matrix. The well-defined nature of the peaks across all samples signifies a high degree of crystallinity. The successful formation of the $BiFeO_3/MoS_2$@MWCNT hybrid is further obvious due to the presence of diffraction peaks corresponding to all three constituent materials: $BiFeO_3$, MoS_2, and MWCNTs.[36] Fig. 1b displays the Rietveld-refined XRD pattern.

The morphology of the prepared composites was investigated by FESEM. Fig. 2(a–e) depicts the morphology of the $BiFeO_3/MoS_2$ binary composite, showing that it is composed of aggregated spherical particles that exhibit a distinctly rough surface texture. These microspheres are densely packed yet form a porous, interconnected network. This specific architectural arrangement is advantageous for electrochemical applications, as the inherent porosity promotes enhanced electrolyte penetration and provides a substantial number of accessible active sites for redox reactions. The observed surface roughness and porous nature collectively suggest a high specific surface area, a key factor for superior electrochemical performance.[37] Fig. 2(f) presents the characteristic morphology of the pristine

MWCNTs, which appear as one-dimensional nanowire-like structures. Their fibrous morphology and excellent intrinsic electrical conductivity make them ideal for constructing efficient electron conduction pathways within a composite material. The structure of the ternary hybrid is revealed in Fig. 2(g–i). The images clearly show that the MWCNTs are evenly distributed and interwoven with the $BiFeO_3/MoS_2$ spheres, creating a cohesive and continuous three-dimensional framework. The carbon nanotubes are embedded within and around the spherical particles, effectively forming a conductive bridge which interlinks the components of the composite material. This integrated structure is anticipated to significantly boost the overall electrical conductivity, provide structural reinforcement, and facilitate rapid charge transport, leading to high electrochemical performance.[38]

The elemental distribution within the $BiFeO_3/MoS_2$@MWCNT composite was verified by energy-dispersive X-ray spectroscopy (EDS) mapping, as presented in Fig. S2(a–f) (SI). The results reveal a highly homogeneous dispersal of bismuth (Bi), iron (Fe), oxygen (O), molybdenum (Mo), sulfur (S), and carbon (C)—across the sampled area. The consistent signals for O, Fe, and Bi confirm the synthesis and even distribution of $BiFeO_3$ nanoparticles. Similarly, the co-location of S and Mo signals substantiates the effective integration of MoS_2 into the hybrid matrix. Furthermore, a pervasive and continuous carbon signal delineates the presence of the MWCNTs, indicating that they form a pervasive and interconnected conductive web throughout the structure. This uniform co-distribution of all
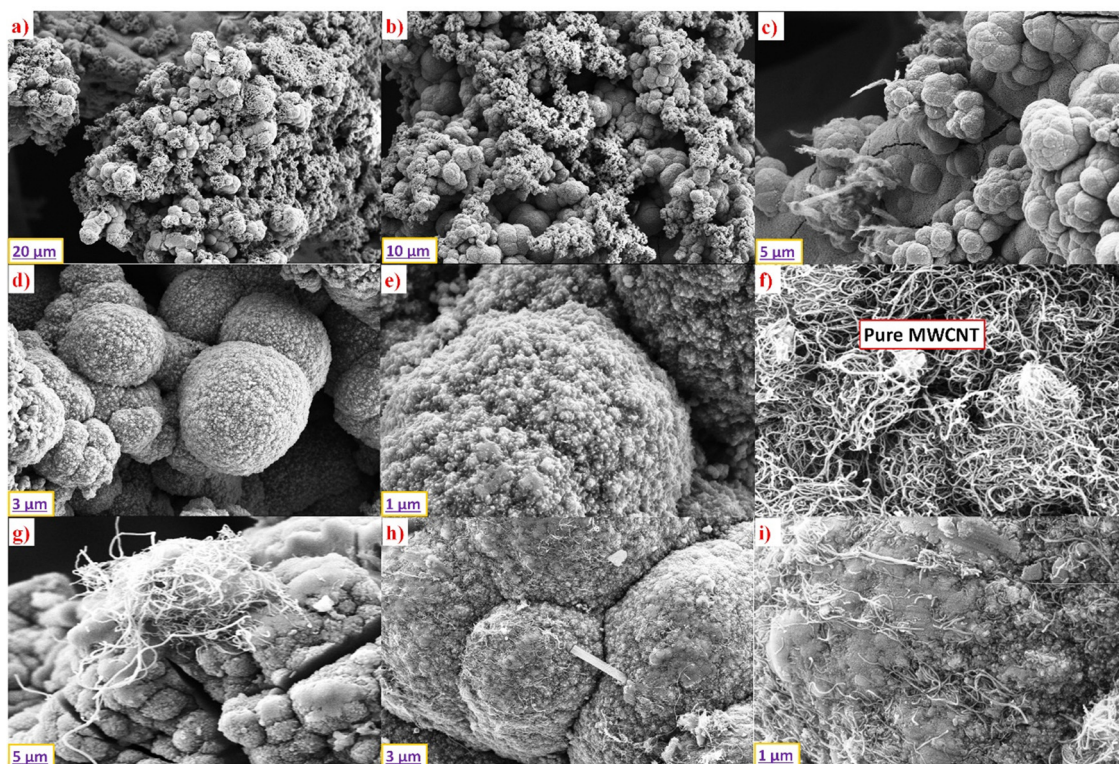

Fig. 2 FESEM micrographs displaying the surface morphology of (a)–(e) $BiFeO_3/MoS_2$, (f) MWCNTs, and (g)–(i) $BiFeO_3/MoS_2$@MWCNT.

elements affirms the creation of a thoroughly integrated hybrid architecture, a characteristic that is highly advantageous for electrochemical applications as it promotes efficient charge transfer pathways and reinforces the electrode's mechanical stability. The EDX spectrum (Fig. S3) confirms the successful formation of the CNTs/BiFeO$_3$–MoS$_2$ composite, showing distinct elemental peaks of C, O, Fe, Mo, S, and Bi at their respective characteristic energies. The atomic % distribution (O 29.8%, C 22.4%, Bi 14.4%, Fe 12.5%, S 11.7%, Mo 9.2%) matches well with the expected composition, indicating successful elemental integration without impurities.

The textural characteristics and porous nature of the synthesized BiFeO$_3$/MoS$_2$ and BiFeO$_3$/MoS$_2$@MWCNT composites were probed using nitrogen physisorption measurements, with the resulting isotherms displayed in Fig. 3(a–d). The adsorption–desorption profiles for both samples conform to Type IV isotherms, which are indicative of mesoporous solids and suggest the presence of larger macropores, likely originating from interparticle spacing or structural defects. Pore size distribution, derived from the adsorption branch via the Barrett–Joyner–Halenda (BJH) method, confirms this porous architecture. The integration of MWCNTs is shown to markedly alter the composite's surface area and pore structure. The Brunauer–Emmett–Teller (BET) surface area for the BiFeO$_3$/MoS$_2$@MWCNT hybrid was calculated to be 221.56 m^2 g^{-1},

representing a noticeable increase compared to the 137.8 m^2 g^{-1} measured for the binary BiFeO$_3$/MoS$_2$ composite.[39] This augmentation can be attributed to the tubular, fibrous form of the MWCNTs, which collaborate to generate an extensive and interlinked porous matrix.

A notable observation is the larger average pore diameter found in the BiFeO$_3$/MoS$_2$@MWCNT hybrid (9.07 nm) relative to the binary composite (5.921 nm). This increase may stem from the formation of new, larger interstitial pores created by the entanglement of MWCNTs with the spherical particles, even as the MWCNTs themselves contribute microporosity, leading to a complex pore system.[40] Furthermore, the integration of structurally sound and uniformly distributed MWCNTs is anticipated to enhance the composite's mechanical strength and overall structural durability. Collectively, the increased specific surface area combined with the developed mesoporosity in the BiFeO$_3$/MoS$_2$@MWCNT composite is predicted to promote more effective electrolyte ion permeation and bolster electron transfer kinetics, rendering it highly suitable for supercapacitor electrode applications.

X-ray photoelectron spectroscopy (XPS) was employed to probe the states of the constituent elements within the BiFeO$_3$/MoS$_2$@MWCNT hybrid. The survey scan confirmed the presence of Bi, Fe, O, Mo, S, and C, and the high-resolution core-level spectra for each are presented in Fig. 4.
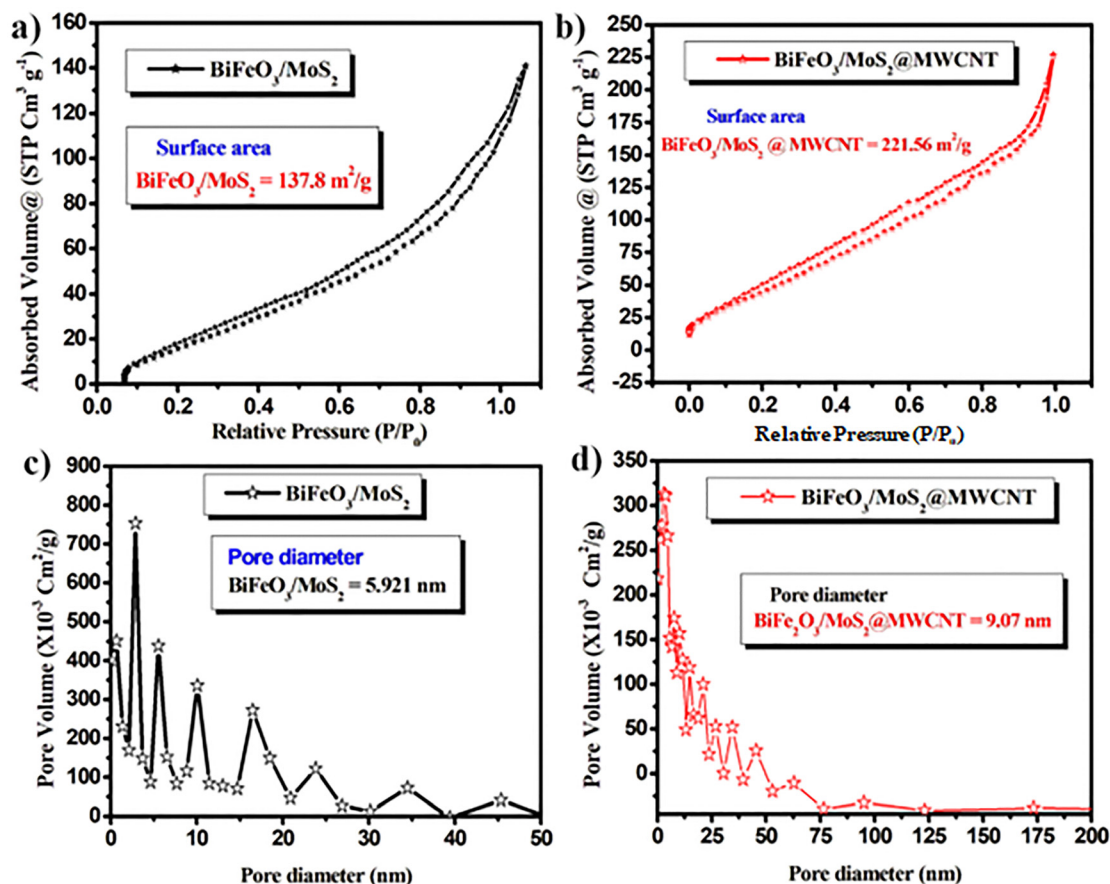

Fig. 3 (a) and (b) BET isotherms and (c) and (d) associated pore size distributions determined by the BJH method for the synthesized composites.
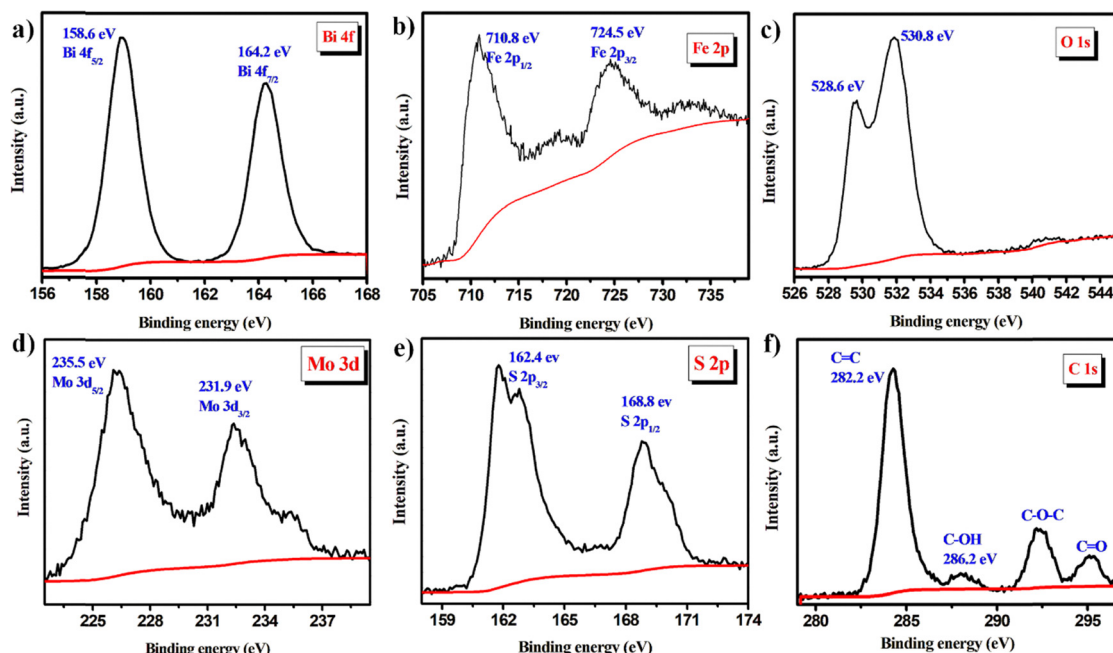
Fig. 4 High-resolution X-ray photoelectron spectroscopy analysis showing core-level signals for constituent elements in the BiFeO$_3$/MoS$_2$@MWCNT hybrid: (a) bismuth 4f, (b) iron 2p, (c) oxygen 1s, (d) molybdenum 3d, (e) sulfur 2p, and (f) carbon 1s.

The Bi 4f spectrum (Fig. 4a) is defined by a well-resolved spin-orbit doublet, with peaks centered at binding energies of 158.6 eV and 164.2 eV, corresponding to the Bi 4f$_{7/2}$ and Bi 4f$_{5/2}$ levels, respectively. The measured splitting of 5.6 eV is characteristic of bismuth in the +3 oxidation state (Bi^{3+}). The Fe 2p spectrum (Fig. 4b) exhibits two primary peaks at 710.8 eV (ion 2p$_{3/2}$) and 724.5 eV (iron 2p$_{1/2}$), confirming the oxidized state of iron. The 13.7 eV separation of the spin-orbit is typical for Fe^{3+}. Deconvolution of the 2p$_{3/2}$ region proclaims contributing components at 709.4 and 711.5, assigned to Fe^{3+} and Fe^{2+}, respectively, indicating the coexistence of both oxidation states. Supporting satellite features are also observed at 718.5 eV and 731.4 eV for Fe^{3+} and at 714.8 eV and 727.1 eV for Fe^{2+}. The O 1s spectrum (Fig. 4c) was deconvoluted into three constituent peaks. The dominant peak at 528.6 eV is attributed to O^{2-} within the Fe–O bonds of the perovskite BFO structure. A second component at 530.8 eV is commonly associated with oxygen in surface hydroxyl groups or oxygen vacancies. A third, broader peak suggests that adsorbed water molecules are present.[41] Analysis of the Mo 3d region (Fig. 4d) shows a doublet at 231.9 eV (Mo 3d$_{3/2}$) and 225.5 eV (Mo 3d$_{5/2}$), which is a definitive signature of Mo^{4+} in MoS$_2$. An additional minor peak is identified as the S 2s orbital, further corroborating the presence of molybdenum sulfide. The S 2p spectrum (Fig. 4e) displays a doublet at 162.4 eV (S 2p$_{3/2}$) and 168.8 eV (S 2p$_{1/2}$), affirming the existence of divalent sulfide ions (S^{2-}). A slight shoulder near 164.7 eV relates to C–S bonds, pointing to a chemical interaction between the MoS$_2$ nanosheets and the carbon nanotube network.[42] Finally, the C 1s spectrum (Fig. 4f) was fitted with peaks at 282.2 eV (C=C, graphitic carbon), 286.2 eV (C–OH/C–O), and 291.7 eV (C–O–C). The slightly asymmetric shape of the main peak is common in

MWCNTs.[43] The integrated MWCNTs enhance the composite's electrical conductivity *via* the delocalized π-electron system of their sp^2-hybridized carbon lattice, which is instrumental in facilitating superior conductivity and boosting electrochemical efficacy.

4. Electrochemical study

4.1 Three-cell configuration

To evaluate the electrochemical performance of the fabricated electrodes, a comprehensive set of electrochemical tests was conducted. Cyclic voltammetry (CV) analysis was performed in a 1 M KOH aqueous electrolyte within a potential window of 0 to 0.6 V (*vs.* Ag/AgCl), utilizing scan rates ranging from 10 to 50 mV s^{-1}. The resulting CV profiles for the BiFeO$_3$/MoS$_2$ and BiFeO$_3$/MoS$_2$@MWCNT electrodes are presented in Fig. 5a and b, respectively. Both composites display well-defined pairs of oxidation and reduction peaks, which are characteristic of faradaic pseudocapacitance driven by reversible redox reactions. The fact that the CV curves retain their shape even at elevated scan rates signifies rapid reaction kinetics and highly efficient ion diffusion within the electrode's structure. This redox activity is principally ascribed to the reversible valence changes of transition metal ions, specifically Fe^{3+}/Fe^{2+} and Mo^{4+}/Mo^{6+}, which occur in tandem with the insertion and extraction of protons (H$^+$) or hydroxide ions (OH$^-$). The interaction of the BiFeO$_3$/MoS$_2$@MWCNT composite can be described as:

$$Fe^{3+} + e^- \leftrightarrow Fe^{2+} \quad MoS_2 + OH^- \leftrightarrow MoO_x + S + e^-$$
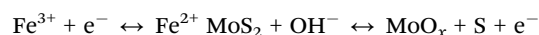
These reversible redox reactions are fundamental to the composite's pronounced faradaic activity and its overall
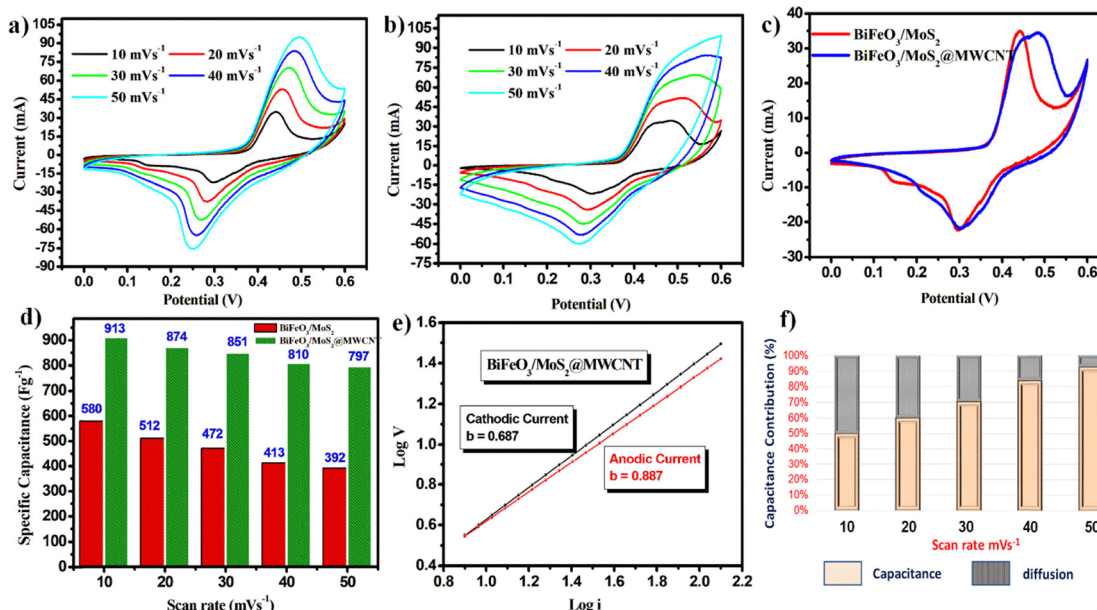
Fig. 5 (a) Cyclic voltammetry profiles of BiFeO$_3$/MoS$_2$; (b) CV curves of BiFeO$_3$/MoS$_2$@MWCNT; (c) comparative CV analysis of both electrode materials; (d) specific capacitance calculated using CV results; (e) determination of b-values from the logarithmic current *versus* scan rate relationship for BiFeO$_3$/MoS$_2$@MWCNT; (f) quantitative analysis of capacitive and diffusion-controlled contributions to charge storage in BiFeO$_3$/MoS$_2$@MWCNT.

pseudocapacitive charge storage mechanism. A direct comparison of the cyclic voltammetry profiles for the BiFeO$_3$/MoS$_2$ and BiFeO$_3$/MoS$_2$@MWCNT electrodes, recorded at a scan rate of 10 mV s^{-1}, is provided in Fig. 5c. The ternary BiFeO$_3$/MoS$_2$@MWCNT composite exhibits a substantially larger integrated CV area and more intense redox peaks than its binary counterpart, providing clear evidence of its greater charge storage capacity and enhanced electrochemical activity. This performance boost is directly enabled by the multifunctional role of the integrated MWCNTs, which elevate the composite's electrical conductivity, furnish mechanical reinforcement, and create a hierarchical network that promotes the rapid transition of both ions and electrons throughout the electrode matrix.

The specific capacitance was calculated using:

$$C_s = \frac{1}{m\nu\Delta V}\int_{v_i}^{v_f} I(V)\mathrm{d}V \tag{1}$$

C_s is the specific capacitance (F g^{-1}), m is the mass of the active material (g), ν is the scan rate (V s^{-1}) and V is the voltage window. To gain deeper insight, the power-law relationship ($i_p = a\nu^b$) was applied on the CV data, as shown in Fig. 5e. The calculated b-value for the cathodic current of the BiFeO$_3$/MoS$_2$@MWCNT electrode was 0.68, while the anodic b-value was significantly higher at 0.887. This disparity indicates a more pronounced surface-controlled (capacitive) charge storage mechanism during the oxidation process, underscoring the increased capacitive features imparted by the MWCNTs. A quantitative deconvolution of the charge storage mechanisms was further performed employing the equation $i(V) = k_1\nu + k_2\nu^{1/2}$ (Fig. 5f). The capacitive contribution constituted 47.96% of the total charge storage at a slow scan rate of 10 mV s^{-1} for the

hybrid composite. This proportion increased markedly to 83.54% at 0.1 V s^{-1}, signifying that capacitive processes become dominant at higher rates. The diffusion insertions, which involve slower ion intercalation into the material bulk, were prevalent at lower scan rates. This affirms that a hybrid mechanism that synergistically combines surface-capacitive effects with diffusion-limited faradaic processes, with the overall kinetics being significantly accelerated by the conductivity and surface area enhancements, resulted in superior performance. The significant enhancement in the capacitive-controlled contribution observed for the BiFeO$_3$/MoS$_2$/MWCNT electrode can be directly attributed to the multifaceted role of the incorporated carbon nanotubes. Firstly, the MWCNTs form a highly conductive, three-dimensional network that permeates the composite, drastically reducing the overall electrical resistance. This efficient "electron highway" ensures rapid charge collection and delivery, which is a fundamental requirement for the fast, surface-dominated kinetics that characterize capacitive behaviour. Secondly, the intertwined MWCNTs prevent the aggregation of BiFeO$_3$ and MoS$_2$ nanoparticles, maintaining a high electrochemically active surface area and creating a porous hierarchical structure. Consequently, the integration effectively 'wires up' the pseudocapacitive components, shifting the charge storage mechanism from a diffusion-limited process to a more capacitive-dominated one.

The charge storage capability was further assessed through galvanostatic charge–discharge (GCD) measurements conducted using a 0 to 0.6 V potential range at current densities between 1 and 5 A g^{-1} as shown in Fig. 6a–d. The BiFeO$_3$/MoS$_2$@MWCNT hybrid demonstrated longer discharge durations relative to the BiFeO$_3$/MoS$_2$ material, revealing
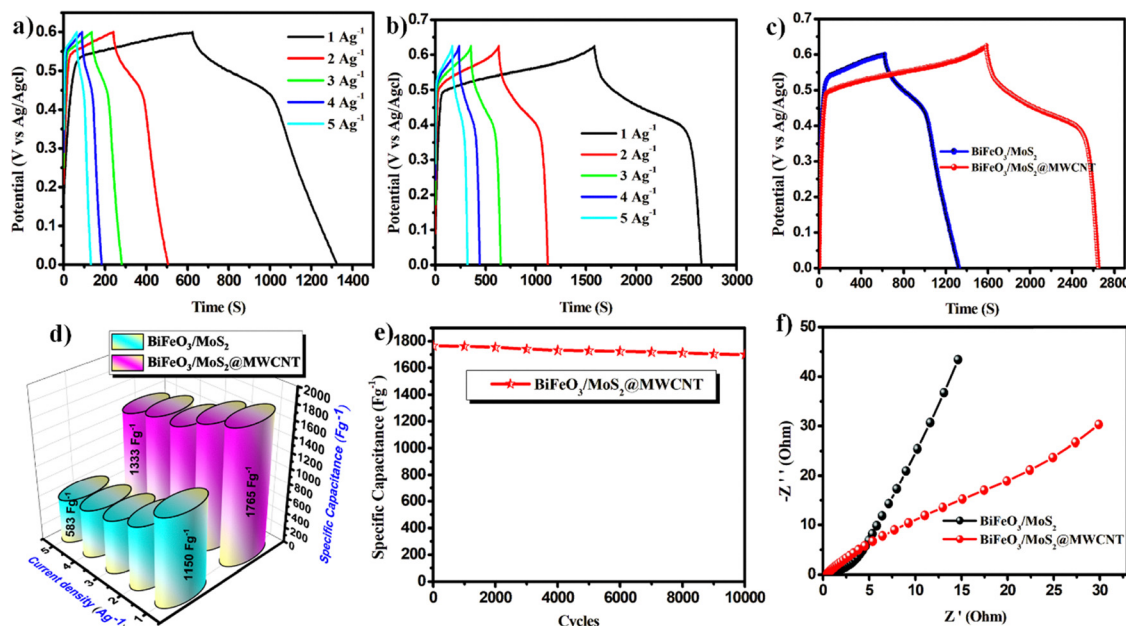
Fig. 6 (a) and (b) Galvanostatic charge–discharge profiles for $BiFeO_3/MoS_2$ and $BiFeO_3/MoS_2$@MWCNT electrodes; (c) comparative charge–discharge curves measured at 1 A g^{-1}; (d) C_s trend at decreasing current densities; (e) stability performance of both composites; (f) Nyquist plots from electrochemical impedance spectroscopy measurements.

better capacitive performance resulting from improved charge transfer and more effective ion dissemination. The C_s was determined from the equation:

$$C_s = \frac{I \times \Delta t}{m \times \Delta V} \qquad (2)$$

A characteristic decline in C_s was observed as the current density increased, a typical phenomenon where the limited time available for ion diffusion at higher rates reduces the accessibility of the material's inner active sites. Despite this trend, the $BiFeO_3/MoS_2$@MWCNT hybrid maintained impressively high C_s values of 1765 F g^{-1} at current densities of 1 A g^{-1}. Table 1 compares these results with previously reported materials.[44–52] In comparison, the $BiFeO_3/MoS_2$ composite displayed lower specific capacitance values of 1150, 833, 705, 640, and 583 F g^{-1} at the respective current densities, demonstrating the advantage of MWCNT integration in enabling faster ion and electron transfer.

The comparative galvanostatic charge–discharge (GCD) profiles recorded at 1 A g^{-1} (Fig. 6d) provide additional confirmation of the enhanced attributes of the $BiFeO_3/MoS_2$@MWCNT. Its charge–discharge curves are more symmetrical and exhibit a substantially longer discharge duration than the binary composite, reflecting superior mechanistic reversibility and improved conductivity. The long-term cycling stability was assessed at a current density of 1 A g^{-1} (Fig. 6e) employing 10 k GCD cycles. The $BiFeO_3/MoS_2$@MWCNT hybrid demonstrated exceptional durability, retaining 96.7% of its original capacitance. This high degree of capacity retention is a direct result of the robust conductive network formed by the MWCNTs, which helps maintain structural integrity during repeated redox reactions. The outstanding cycling performance underscores the composite's remarkable structural stability and highly reversible faradaic character.

The charge-transfer kinetics were investigated using electrochemical impedance spectroscopy (EIS), with the resulting Nyquist plots shown in Fig. 6f. The plots for both materials

Table 1 Performance comparison of specific capacitance and capacitive retention between current investigation and earlier reported studies

| Material	I/m (A g^{-1})	C_s (F g^{-1})	Cyclic performance (no. of cycles)	Synthesis method	Ref.
$CoFe_2O_4$/MWCNT	1	390	93% (2 k)	Sono chemical	44
$Ni(OH)_2$ coating on carbon nanosheet	1	2218	93% (10 k)	Facile preoxidation	45
Copper–$BiFeO_3$	0.5	732	88.64% (5 k)	Solution	48
$BiFeO_3/g\text{-}C_3N_4$	1	330	60% (5 k)	Preoxidation	47
Zinc/$BiFeO_3$	200 m	223	85.8% (10 k)	Solution	46
$BiFeO_3/g\text{-}C_3N_4$	1	1472	87% (3 k)	Preoxidation	49
$BiFeO_3/g\text{-}C_3N_4$	1	1164	(5 k)	Hydrothermal	50
Zinc/$BiFeO_3$//$Bi_{25}FeO_{40}$	1	1087	91% (10 k)	Hydrothermal	52
$BiFeO_3$/graphene	1	306.6	60% (0.3 k)	Chronoamperometric	51
$BiFeO_3/MoS_2$@MWCNT	1	1765	96.7% (10 k)	Hydrothermal	This work

feature a depressed semicircular arc in the high-frequency region, which corresponds to the charge-transfer resistance (R_{ct}) at the electrode–electrolyte interface, followed by a linear slope in the low-frequency region representing the Warburg impedance (W), indicative of ion diffusion processes. The ternary BiFeO$_3$/MoS$_2$@MWCNT electrode exhibited a substantially lower R_{ct} value of 1.23 Ω, compared to 2.68 Ω for the binary BiFeO$_3$/MoS$_2$ composite, signifying a more rapid faradaic charge-transfer process. A minor reduction in the equivalent series resistance (R_s) was also observed for the MWCNT-incorporated sample (0.71 Ω *versus* 1.02 Ω), suggesting improved electrical contact and ionic accessibility at the electrode interface.

These enhancements are directly credited to the incorporation of MWCNTs, which form a highly conductive, percolating network that interlinks the electroactive BiFeO$_3$ and MoS$_2$ particles.[55] This network serves to diminish interparticle contact resistance and promotes deeper electrolyte infiltration. While the layered MoS$_2$ supplies active sites for reversible ion intercalation and redox reactions, the MWCNTs provide a dedicated pathway for electron conduction, thereby reducing

overall internal polarization. The superior performance of the BiFeO$_3$/MoS$_2$@MWCNT hybrid stems from a synergistic interplay: the pseudocapacitive contributions from BiFeO$_3$ and MoS$_2$ are effectively leveraged by the MWCNTs' conductive and porous architecture. Functioning as an electron "superhighway" and a structural reinforcement, the MWCNTs facilitate superior electrolyte access and shorten ion diffusion paths. Moreover, their presence helps passivate surface defects and mitigate undesirable side reactions, which contribute to lower self-discharge and enhanced long-term cycling stability. In summary, the integration of MWCNTs into the BiFeO$_3$/MoS$_2$ composite profoundly improves its capacitive performance, establishing the BiFeO$_3$/MoS$_2$@MWCNT hybrid as a highly promising electrode material for advanced energy storage systems.

4.2 Asymmetric capacitor

To evaluate practical application, an asymmetric supercapacitor (ASC) was constructed, employing the BiFeO$_3$/MoS$_2$@MWCNT hybrid as the positive electrode and activated carbon (AC) as the negative electrode, with a glass microfiber membrane serving as
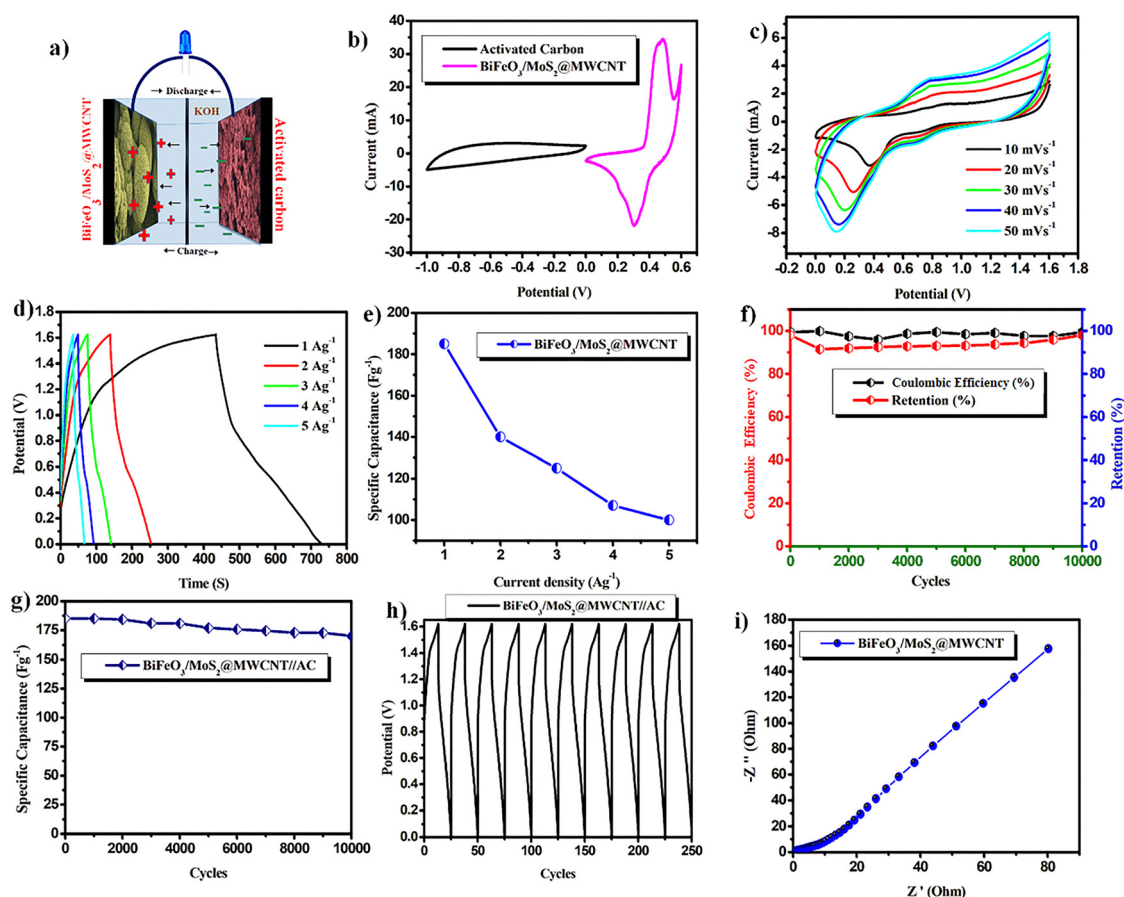
Fig. 7 (a) Schematic representation of the assembled BiFeO$_3$/MoS$_2$@MWCNT//AC asymmetric supercapacitor; (b) comparative cyclic voltammetry curves of BiFeO$_3$/MoS$_2$@MWCNT and AC electrodes at 10 mV s^{-1}; (c) CV profiles of the full asymmetric device at various scan rates; (d) Galvanostatic charge–discharge profiles of the ASC device; (e) C_s at different current densities; (f) capacitance retention and Coulombic efficiency over 10 000 cycles; (g) specific capacitance evolution during the cycling testing; (h) charge–discharge profiles for the initial 250 cycles; (i) electrochemical impedance spectroscopy analysis of the ASC device.

the separator in a 1 M KOH electrolyte. A schematic illustration of this device configuration is provided in Fig. 7a. This design strategically combines the pseudocapacitive charge storage of the BiFeO$_3$/MoS$_2$@MWCNT composite with the electric double-layer capacitive (EDLC) characteristics of AC, enabling the device to achieve an expanded operational voltage window of 1.6 V. The individual cyclic voltammetry profiles of the activated carbon and hybrid composite, recorded at 0.01 V s^{-1} (Fig. 7b), highlight their complementary storage mechanisms: the AC electrode displays a characteristic rectangular shape denoting non-faradaic EDLC behavior, whereas the BiFeO$_3$/MoS$_2$@MWCNT electrode shows pronounced redox peaks, signifying its pseudocapacitive nature. The pronounced interaction of BiFeO$_3$/MoS$_2$@MWCNT with the electrolyte ions stems from synergistic contributions. The BiFeO$_3$ component provides reversible redox reactions, primarily involving the Fe^{3+}/Fe^{2+} couple. This is complemented by the MoS$_2$, which contributes its two-dimensional layered structure that facilitates ion intercalation and offers additional redox activity through Mo^{4+}/Mo^{6+} transitions. The incorporated MWCNTs create a highly conductive matrix that ensures efficient electron transport, enhances mechanical stability, and inhibits the agglomeration of active particles. Furthermore, inherent nitrogen and sulfur moieties, likely derived from the MoS$_2$, improve the electrode's hydrophilicity, thereby enhancing electrolyte wettability and increasing the number of accessible electroactive sites for improved charge storage. The CV curves of the fully assembled ASC device, measured across a range of scan rates (Fig. 7c), retain their profile even as the scan rate increases, indicating rapid ion transport and highly reversible capacitance. These curves display a composite shape, merging a quasi-rectangular form with distinct redox humps, which visually confirms the hybrid energy storage mechanism combining EDLC from the AC and faradaic processes from the positive electrode. The GCD profiles for the assembled asymmetric device, shown in Fig. 7d, exhibit nearly ideal symmetric triangular shapes accompanied by a negligible voltage drop (iR drop). This indicates highly efficient charge–discharge kinetics and very low internal resistance. The C_s of the full cell, calculated from the discharge curves using eqn (2) (which accounts for the total active mass loaded on both electrodes), reached values of 185, 140, 125, 107, and 100 F g^{-1} at current densities of 1, 2, 3, 4, and 5 A g^{-1}, respectively. Furthermore, the device demonstrated an exceptional capacitance retention of 92.5% after cycling (Fig. 7e).

The long-term cycling stability of the asymmetric supercapacitor (ASC) was evaluated over 10 000 consecutive galvanostatic charge–discharge (GCD) cycles at a high current density of 5 A g^{-1}. The device demonstrated exceptional durability, with a capacitive retention of 92.5% and a coulombic efficiency of 99.1% at the end of the test (Fig. 7f and g). The minimal shape change in the GCD curves over the first 250 cycles (Fig. 7h) further validates the outstanding electrochemical reversibility and structural integrity of the device. This robustness is largely attributable to the MWCNT framework and stable BiFeO$_3$/MoS$_2$ heterointerfaces, which collectively mitigate mechanical stress and buffer volume changes during cycling. Electrochemical impedance spectroscopy (EIS) performed after cycling (Fig. 7i)
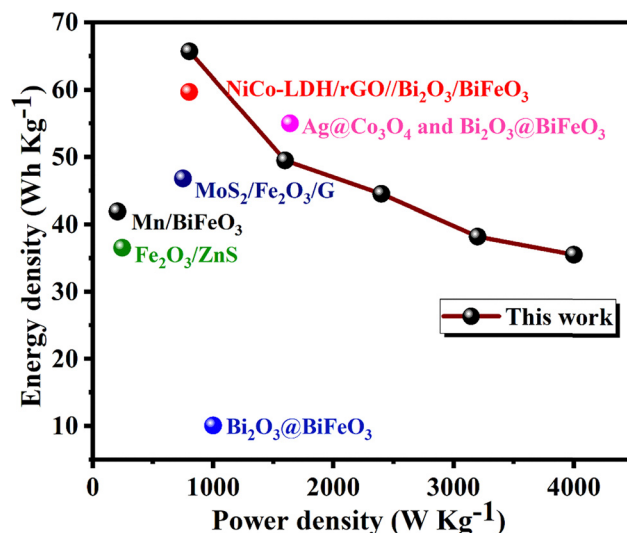

Fig. 8 Ragone plot illustrating the energy-power characteristics of the assembled asymmetric supercapacitor, with comparative performance data from previously reported systems.

revealed minimal degradation, with a solution resistance (R_s) of 1.64 Ω and a charge-transfer resistance (R_{ct}) of 10.8 Ω, while the nearly vertical line in the low-frequency region confirms ideal capacitive behavior with fast ion diffusion. The practical applicability of the device is highlighted by its Ragone plot performance (Fig. 8), delivering a notable energy density of 65.7 Wh kg^{-1} at 802.7 W kg^{-1} power density, while retaining 35.5 Wh kg^{-1} at an elevated power density of 4000 W kg^{-1}. This performance is competitive with, and in several cases superior to, other state-of-the-art systems. For instance, it surpasses the energy densities reported for Mn/BiFeO$_3$ (41.91 Wh kg^{-1}),[53] Fe$_2$O$_3$/ZnS (36.54 Wh kg^{-1}),[57] and MoS$_2$/Fe$_2$O$_3$/G (46.8 Wh kg^{-1}).[58] While the NiCo–LDH/rGO//Bi$_2$O$_3$/BiFeO$_3$ device shows a comparable energy density of 59.7 Wh kg^{-1} at a similar power level,[54] and the Ag@Co$_3$O$_4$ and Bi$_2$O$_3$@BiFeO$_3$ system achieves a high power density of 1640 W kg^{-1},[56] the unique combination of both high energy and high power delivered by our BiFeO$_3$/MoS$_2$@MWCNT hybrid underscores its balanced and advanced performance. The superior metrics achieved in this work highlight the effectiveness of the ternary composite design in synergistically enhancing charge storage capacity and rate capability. These results confirm the efficacy of composite engineering in developing next-generation energy storage systems that harmonize the advantages of batteries and supercapacitors.

5. Conclusion

In conclusion, a strategically engineered ternary hybrid composite comprising BiFeO$_3$, MoS$_2$, and multi-walled carbon nanotubes (BFO/MoS$_2$@MWCNT) has been successfully developed and validated as a highly promising electrode for advanced asymmetric supercapacitors. The layered architecture of MoS$_2$ introduced a high density of electroactive sites for

faradaic reactions, while the integrated network of MWCNTs established a highly conductive pathway that drastically improved electron mobility and ion accessibility throughout the electrode. This synergistic combination effectively overcame the primary limitations of pure $BiFeO_3$, leading to a remarkable enhancement in its overall electrochemical performance. The practical viability of this material was confirmed by constructing an asymmetric device, which coupled the composite positive electrode with an activated carbon negative electrode. This full cell delivered a notable energy density, maintained robust performance under high current loads, and exhibited outstanding cycling stability. This study underscores the efficacy of multi-component composite engineering as a powerful strategy for developing high-performance, durable, and scalable electrode materials, thereby contributing to the advancement of next-generation energy storage technologies.

Conflicts of interest

The authors declare that there is no conflicts of interest regarding the research work reported in this manuscript.

Data availability

The data will be made available on request.

The data supporting this article have been included as part of the supplementary information (SI). Supplementary information is available. See DOI: https://doi.org/10.1039/d5ya00268k.

Acknowledgements

References

1 R. A. Mir, O. A. Sami, S. A. Akbar, A. Uddin, M. M. Alam, M. Z. Ansari and A. A. P. Khan, *Nano Energy*, 2025, **133**, 110446, DOI: 10.1016/j.nanoen.2024.110446.

2 R. K. Maurya, A. K. Shukla, S. K. Srivastava and A. K. Singh, *J. Power Sources*, 2025, **640**, 236818, DOI: 10.1016/j.jpowsour.2024.236818.

3 S. Sahani, H. Mahajan and S. S. Han, *J. Energy Storage*, 2024, **90**, 111808, DOI: 10.1016/j.est.2024.111808.

4 E. Murugan, S. Govindaraju and S. Santhoshkumar, *Electrochim. Acta*, 2021, **392**, 138973, DOI: 10.1016/j.electacta.2021.138973.

5 E. Murugan and F. Lyric, *Nanoscale*, 2025, **17**, 11578, DOI: 10.1039/D5NR00369G.

6 H. H. Hegazy, M. M. El-Desoky, A. G. El-Shamy and M. M. Abutailkh, *RSC Adv.*, 2024, **14**, 32958, DOI: 10.1039/D4RA05680A.

7 M. Xie, Z. Xu, S. Duan, Z. Tian, Y. Zhang, W. Xiang and X. Zhang, *ACS Energy Lett.*, 2016, **1**, 814, DOI: 10.1021/acsenergylett.6b00366.

8 X. Wang, Y. Zhang, J. Liu, H. Li, Z. Li and J. Li, *EcoEnergy*, 2023, **1**, 448, DOI: 10.1002/ece2.19.

9 E. Murugan, K. Munusamy and A. V. Babu, *Chem. Eng. J.*, 2024, **501**, 157473, DOI: 10.1016/j.cej.2024.157473.

10 Y. Yao, D. Zhou, Y. Zhao, Z. Li, J. Li, Z. Liu and L. Li, *J. Colloid Interface Sci*, 2023, **649**, 519, DOI: 10.1016/j.jcis.2023.06.111.

11 S. Jo, S. Pak, Y. W. Lee, S. Cha, J. Hong and J. I. Sohn, *Int. J. Energy Res.*, 2023, **2023**, 2496447, DOI: 10.1155/2023/2496447.

12 V. V. Jadhav and R. S. Mane, *Bismuth-Ferrite-Based Electrochemical Supercapacitors*, Springer Nature, 2020, DOI: 10.1007/978-3-030-37177-7.

13 J. Khan, *RSC Adv.*, 2025, **15**, 37361–37370.

14 X. Li, W. Wang, X. Wang, C. Yang, G. Liu and H. Wang, *J. Energy Storage*, 2024, **103**, 114231, DOI: 10.1016/j.est.2024.114231.

15 N. Matinise, N. Botha, I. G. Madiba and M. Maaza, *MRS Adv.*, 2023, **8**, 703, DOI: 10.1557/s43580-023-00548-8.

16 S. Yin, S. Wu, J. Chen, Z. Chen, H. Hou, Q. Liu, Y. Wang and W. Zhang, *Funct. Mater. Lett.*, 2018, **11**, 1850013, DOI: 10.1142/S179360471850013X.

17 M. A. Mumtaz, A. M. Afzal, M. H. Waris, M. Ali, M. W. Iqbal, A. S. Alqarni and S. A. Issa, *Synth. Met.*, 2025, **311**, 117818, DOI: 10.1016/j.synthmet.2024.117818.

18 N. Joseph, P. M. Shafi and A. C. Bose, *Energy Fuels*, 2020, **34**, 6558, DOI: 10.1021/acs.energyfuels.0c00746.

19 M. Ali, A. M. Afzal, M. W. Iqbal, S. Mumtaz, M. Imran, F. Ashraf, A. U. Rehman and F. Muhammad, *Int. J. Energy Res.*, 2022, **46**, 22336, DOI: 10.1002/er.8592.

20 M. A. Kosnan, M. A. Azam, N. E. Safie, R. F. Munawar and A. Takasaki, *Micromachines*, 2022, **13**, 1837, DOI: 10.3390/mi13111837.

21 S. Sharifi, K. Rahimi and A. Yazdani, *J. Energy Storage*, 2023, **72**, 108499, DOI: 10.1016/j.est.2023.108499.

22 M. Li, Z. Li, X. Wang, N. Fu and Z. Yang, *J. Electroanal. Chem.*, 2022, **919**, 116556, DOI: 10.1016/j.jelechem.2022.116556.

23 A. W. Alrowaily, H. A. Alyousef, B. M. Alotaibi, M. F. Alotiby, A. G. Al-Sehemi, K. Ahmad, A. M. Henaish and F. A. Al-Zahrani, *Mater. Chem. Phys.*, 2024, **322**, 129517, DOI: 10.1016/j.matchemphys.2024.129517.

24 R. Zhao, J. Wang and Y. Han, *J. Chem. Res.*, 2024, **48**(1), 1–10, DOI: 10.1177/17475198241231534.

25 A. Tundwal, H. Kumar, B. J. Binoj, R. Sharma, G. Kumar, R. Kumari, A. Dhayal, A. Yadav, D. Singh and P. Kumar, *RSC Adv.*, 2024, **14**, 9406, DOI: 10.1039/D4RA00513G.

26 M. Z. Iqbal, *Electrochim. Acta*, 2021, **368**, 137529, DOI: 10.1007/s11581-025-05911-9.

27 S. Zainab, S. U. Awan, D. Hussain, S. Rizwan, T. Iqbal and M. Azeem, *J. Energy Storage*, 2025, **126**, 116947, DOI: 10.1016/j.est.2025.116947.

28 A. Baby, V. Tejashwini, S. P. Balakrishnan, M. Afzal and J. Cherusseri, *Synth. Met.*, 2024, **308**, 117714, DOI: 10.1016/j.synthmet.2024.117714.

29 N. Jhanjhariya and S. Lata, *J. Energy Storage*, 2024, **82**, 110577, DOI: 10.1016/j.est.2024.110577.

30 H. Nawaz, J. Iqbal, S. Jabeen, M. I. Shahzad and N. Ahmad, *J. Alloys Compd.*, 2025, 180773, DOI: 10.1016/j.jallcom.2025.180773.

31 S. M. Yahaya, N. Abdu, I. A. Aliyu and B. Mukhtar, *Commun. Soil Sci. Plant Anal.*, 2025, **56**(10), 1539–1554.

32 A. Baby, V. Tejashwini, S. P. Balakrishnan, M. Afzal and J. Cherusseri, *Synth. Met.*, 2024, **308**, 117714, DOI: 10.1016/j.synthmet.2024.117714.

33 Q. Chen, F. Xie, G. Wang, K. Ge, H. Ren, M. Yan, Q. Wang and H. Bi, *Ionics*, 2021, **27**, 4083, DOI: 10.1007/s11581-021-04175-x.

34 S. Hussain, I. Rabani, D. Vikraman, A. Feroze, M. Ali, Y. S. Seo, W. Song, K. S. An, H. S. Kim, S. H. Chun and J. Jung, *Chem. Eng. J.*, 2021, **421**, 127843, DOI: 10.1016/j.cej.2020.127843.

35 L. Zhang, X. Li, J. Chen, D. Jin and J. Cheng, *Ceram. Int.*, 2022, **48**, 15908, DOI: 10.1016/j.ceramint.2022.03.152.

36 P. Tiwari, D. Janas and R. Chandra, *Carbon*, 2021, **177**, 291, DOI: 10.1016/j.carbon.2021.02.080.

37 V. Molahalli, G. Soman, V. S. Bhat, M. S. Jyothi, U. Sirimahachai, S. Maradur, P. De Padova, N. Chattham and G. Hegde, *Nano Express*, 2024, **5**, 035006, DOI: 10.1088/2632-959X/ad5b7f.

38 W. Sheng, W. Hanbo, P. Dongyu, W. Ziming, F. Zhitian, Y. Mingrui, L. Kechang and L. Haiyan, *Surf. Interfaces*, 2024, **46**, 104049, DOI: 10.1016/j.surfin.2024.104049.

39 N. Tanapongpisit, P. Wongprasod, P. Laohana, S. Sonsupap, J. Khajonrit, S. Musikajaroen, U. Wongpratat, B. Yotburut, S. Maensiri, W. Meevasana and W. Saenrang, *Sci. Rep.*, 2024, **14**, 27811, DOI: 10.1038/s41598-024-78061-9.

40 B. M. Al-Maswari, *ACS Omega*, 2023, **8**, 16145, DOI: 10.1021/acsomega.2c07694.

41 Q. Pan, C. Yang, Q. Jia, W. Qi, H. Wei, M. Wang, S. Yang and B. Cao, *Chem. Eng. J.*, 2020, **397**, 125524, DOI: 10.1016/j.cej.2020.125524.

42 X. Sun, Y. A. Pang, S. Li, Y. Yu, X. Ding, L. Wang and Q. Zhang, *Ceram. Int.*, 2022, **48**, 21317, DOI: 10.1016/j.ceramint.2022.04.106.

43 C. Qin, L. Cao, Z. Fang, F. Lai, M. Yao, Z. Lin and P. Zhang, *Ionics*, 2021, **27**, 1757, DOI: 10.1007/s11581-021-03934-0.

44 J. Acharya, B. G. Raj, T. H. Ko, M. S. Khil, H. Y. Kim and B. S. Kim, *Int. J. Hydrogen Energy*, 2020, **45**, 3073, DOI: 10.1016/j.ijhydene.2019.11.145.

45 M. Xie, Z. Xu, S. Duan, Z. Tian, Y. Zhang, W. Xiang and X. Zhang, *Nano Res.*, 2018, **11**, 216, DOI: 10.1007/s12274-017-1624-1.

46 S. Yu, C. Yang, W. Wang, D. Han, W. Qi, R. Ling, S. Xu and G. Liu, *J. Ind. Eng. Chem.*, 2024, **138**, 415, DOI: 10.1016/j.jiec.2024.04.032.

47 H. Pecenek, F. K. Dokan, M. S. Onses, E. Yılmaz and E. Sahmetlioglu, *J. Energy Storage*, 2023, **64**, 107075, DOI: 10.1016/j.est.2023.107075.

48 A. Ramadan and W. Ramadan, *J. Energy Storage*, 2024, **100**, 113702, DOI: 10.1016/j.est.2024.113702.

49 B. S. Reghunath, S. Rajasekaran, K. R. Sunaja Devi, B. Saravanakumar, J. J. William, D. Pinheiro, D. Govindarajan and S. Kheawhom, *J. Phys. Chem. Solids*, 2022, **171**, 110985, DOI: 10.1016/j.jpcs.2022.110985.

50 T. Zahra, A. Gassoumi, S. Gouadria, M. Abdullah, F. F. Alharbi, S. Aman and H. M. Farid, *Diamond Relat. Mater.*, 2024, **144**, 110927, DOI: 10.1016/j.diamond.2024.110927.

51 P. Pattananuwat and A. Khampuanbut, *Electrochim. Acta*, 2021, **370**, 137741, DOI: 10.1016/j.electacta.2020.137741.

52 Y. Selvaraj, K. Paramasivam, M. C. Franklin, K. Sivalingam Nallathambi, V. Elayappan and H. Kuzhandaivel, *J. Phys. Chem. C*, 2024, **128**, 5418, DOI: 10.1021/acs.jpcc.3c07844.

53 K. A. Geelani, B. M. Alotaibi, A. W. Alrowaily, H. A. Alyousef, M. F. Alotiby, M. Abdullah and A. Dahshan, *J. Energy Storage*, 2024, **85**, 111054, DOI: 10.1016/j.est.2024.111054.

54 X. Xu, S. Wu, X. Sun, S. Tian, C. Liu, P. Zhang, S. Fu, Y. Wang, Q. Su, X. Wang and Q. Yang, *J. Energy Storage*, 2023, **72**, 108530, DOI: 10.1016/j.est.2023.108530.

55 N. Senthilkumar, Y. Selvaraj, N. Eswaramoorthy, S. Pandiaraj, K. A. Alibrahim and A. N. Alodhayb, *Colloids Surf., A*, 2024, **695**, 134189, DOI: 10.1016/j.colsurfa.2024.134189.

56 B. Hu, J. Jiang, P. Wang, H. Cheng, D. Li, Z. Zhou, Y. Deng, N. Zhao, X. Yuan and Z. Li, *ACS Appl. Nano Mater.*, 2024, **8**, 720, DOI: 10.1021/acsanm.3c04910.

57 M. Hadi, *Inorg. Chem. Commun.*, 2025, **177**, 114323, DOI: 10.1016/j.inoche.2025.114323.

58 R. Palanisamy, D. Karuppiah, S. Venkatesan, S. Mani, M. Kuppusamy, S. Marimuthu, A. Karuppanan, R. Govindaraju, S. Marimuthu, S. Rengapillai and M. Abdollahifar, *Colloid Interface Sci. Commun.*, 2022, **46**, 100573, DOI: 10.1016/j.colcom.2021.100573.